

Computational Aeroacoustics based on Lighthill's Acoustic Analogy

Manfred Kaltenbacher¹, Max Escobar², Stefan Becker³, and Irfan Ali⁴

¹ Friedrich–Alexander–Universität Erlangen–Nürnberg, Lehrstuhl für Sensorik,
Paul–Gordan–Straße 3/5, 91052 Erlangen, Germany
manfred@lse.eei.uni-erlangen.de

² Friedrich–Alexander–Universität Erlangen–Nürnberg, Lehrstuhl für Sensorik,
Paul–Gordan–Straße 3/5, 91052 Erlangen, Germany
max.escobar@lse.eei.uni-erlangen.de

³ Friedrich–Alexander–Universität Erlangen–Nürnberg, Lehrstuhl für Strömungsmechanik,
Cauerstraße 4, 91058 Erlangen, Germany
sbecker@lstm.uni-erlangen.de

⁴ Friedrich–Alexander–Universität Erlangen–Nürnberg, Lehrstuhl für Strömungsmechanik,
Cauerstraße 4, 91058 Erlangen, Germany
irfan@lstm.uni-erlangen.de

Summary. Aeroacoustics is concerned with sound, generated by turbulent fluid motion or aerodynamic forces interacting with surfaces. Although no complete scientific theory of the generation of noise by aerodynamic flows has been established, most practical aeroacoustic analysis relies upon the so-called *Acoustic Analogy*, whereby the governing equations of fluid dynamics are rewritten into a wave like equation. The most common and a widely-used formulation is Lighthill's aeroacoustic analogy, which was proposed by James Lighthill in the 1950s, when studying noise, generated by jet engines. Computational Aeroacoustics (CAA) is the application of numerical methods to find approximate solutions of the governing equations for specific aeroacoustic problems. Most of the proposed methods numerically solved on high performance computers (HPC), are employed in a hybrid two-step approach. The first step consists in computing the turbulent flow field from which the acoustic source terms are evaluated. Subsequently the acoustic radiation is computed. Therewith, no feedback from the acoustic field to the turbulent flow is considered.

4.1 Introduction

In the last years, manufacturers have started to consider the aerodynamic noise level in many industrial applications as a relevant design parameter (e.g. airplanes, wind turbines, cars, air conditioning systems, etc.). Because of this growing demand for reducing noise levels and for fulfilling noise regulations, there is a great motivation to investigate in basic aeroacoustic phenomena and mechanisms of sound generation and propagation. Besides experimental methods, a great need exists to develop numerical tools to simulate aeroacoustic phenomena.

Since the beginning of computational aeroacoustics several numerical methodologies have been proposed, each of these trying to overcome the challenges that the specific problems under investigation pose for an effective and accurate computation of the radiated sound. The main difficulties which have to be considered for the simulation of flow noise problems include [9, 26]:

- *Energy disparity and acoustic inefficiency:* There is a large disparity between the energy of the flow in the non-linear field and the acoustic energy in the far field (the hydrodynamic pressure p is in the range of $10^4 - 10^6$ Pa, whereas the acoustic pressure p' is in the range of $10^{-5} - 10$ Pa). Therefore, the radiated acoustic energy of an unsteady flow is a very small fraction of the total energy in the flow. In general, the total radiated power of a turbulent jet scales with $O(U^8/c_0^5)$, and for a dipole source arising from pressure fluctuations on surfaces inside the flow scales with $O(U^6/c_0^3)$, where U denotes the characteristic flow velocity and c_0 the speed of sound.
- *Length scale disparity:* Large disparity also occurs between the size of an eddy in the turbulent flow and the wavelength of the generated acoustic noise. Low Mach number eddies have a characteristic length scale l , velocity U , an integral time scale l/U and a frequency ω . This eddy will then radiate acoustic waves of the same characteristic frequency, but with a much larger length scale, expressed by the acoustic wavelength λ

$$\lambda \propto c_0 \frac{l}{U} = \frac{l}{M}.$$

- *Preservation of multipole character:* The numerical analysis must preserve the multipole structure of the acoustic source, which applies to quadrupoles representing turbulent eddies or forces acting on a surface inside the flow. In order to estimate the source strength, it is necessary to resolve the whole structure of the source.
- *Dispersion and dissipation:* Any discrete form of the acoustic wave equation cannot precisely represent the dispersion relation of the acoustic sound. Numerical discretization in space and time converts the original non-dispersive system into a dispersive discretized one, which exhibits wave phenomena of two kinds:
 1. Long wavelength components approaching the solution of the original partial differential equation as the grid is refined.
 2. Short wavelength components (spurious waves) without counterpart in the original equation evolving in the numerical scheme disturbing the solution.
 The wave equation shows a non-dissipative behavior; as such, dissipative errors must be avoided by a numerical scheme, in which both the amplitude and phase of the wave are of crucial importance [2, 8].
- *Flows with high Mach and Reynolds number:* Aeroacoustic problems often involve both high Mach and high Reynolds numbers. Flows at a high Mach number may induce new non-linear sources and convective effects while flows at a high Reynolds number introduce multiple scale difficulties due to the disparity between the acoustic wavelength λ and the size of the energy dissipating eddies.

- *Simulation of unbounded domains:* As a main issue for the simulation of unbounded domains using volume discretization methods remains the boundary treatment which needs to be applied to avoid the reflection of the outgoing waves on the truncating boundary of the computational domain. This remains to be a very active field of research and several numerical formulations have been developed for both transient and harmonic analyses.

Currently available aeroacoustic methodologies overcome only some of these broad range of physical and numerical issues, which restricts their applicability, making them, in many cases, problem dependent methodologies. The application of Direct Numerical Simulation (DNS) is becoming more feasible with the permanent advancement in computational resources. However, due to the large disparities of length and energy scales between fluid and acoustic fields, DNS remains restricted to low Reynolds number flows. In a DNS, all relevant scales of turbulence are resolved and no turbulence modeling is employed. Some relevant work has been done in this direction by Freund [21], however, the simulation of practical problems involving high Reynolds numbers requires very high resolutions which are still far beyond the capabilities of current supercomputers [52]. In this respect, more recently a promising heterogeneous domain decomposition technique [51] has been proposed, as a way to overcome the scales disparities and still allow a direct simulation. In this manner, the equations, numerical methods, grids, and time steps within each subdomain could be adapted to meet the local physical requirements. Meanwhile, hybrid methodologies still remain as the approach most commonly used for aeroacoustic computations, due to the practical advantages provided by the separate treatment of fluid and acoustic computations. In these schemes, the computational domain is split into a non-linear source region and a wave propagation region, and different physical models are used for the flow and acoustic computations. Herewith, first a turbulence model is used to compute the unsteady flow in the source region. Secondly, from the fluid field, acoustic sources are evaluated, which are used as input for the computation of the acoustic propagation. Therewith, a common aspect to hybrid methodologies lies in the assumption that no significant physical influence occurs from the acoustic propagation to the flow field.

Figure 4.1 shows the typical numerical methods which are employed when using any of these hybrid methodologies. For a precise prediction of the flow induced noise, Large Eddy Simulation (LES) is mainly used for solving the flow and providing the acoustic sources. In the LES method the large scales are directly resolved and the effect of the small scales on the large scales are modeled [7]. Although still with a relatively high computational cost, with the LES method it is possible to simulate turbulent flows with high Reynolds numbers and complex geometries. Therefore, this method has been adopted by researchers as one of the standard methods for computing the turbulent near field in CAA problems. Additionally we find the group of combined RANS (Reynolds Averaged Navier Stokes)/LES methods [24]. This type of methods blend statistical approaches with LES, in order to yield enhanced predictions of both turbulence statistics and unsteady flow dynamics at a fraction of the cost of traditional LES. Under these RANS/LES methods we find Detached Eddy Simu-

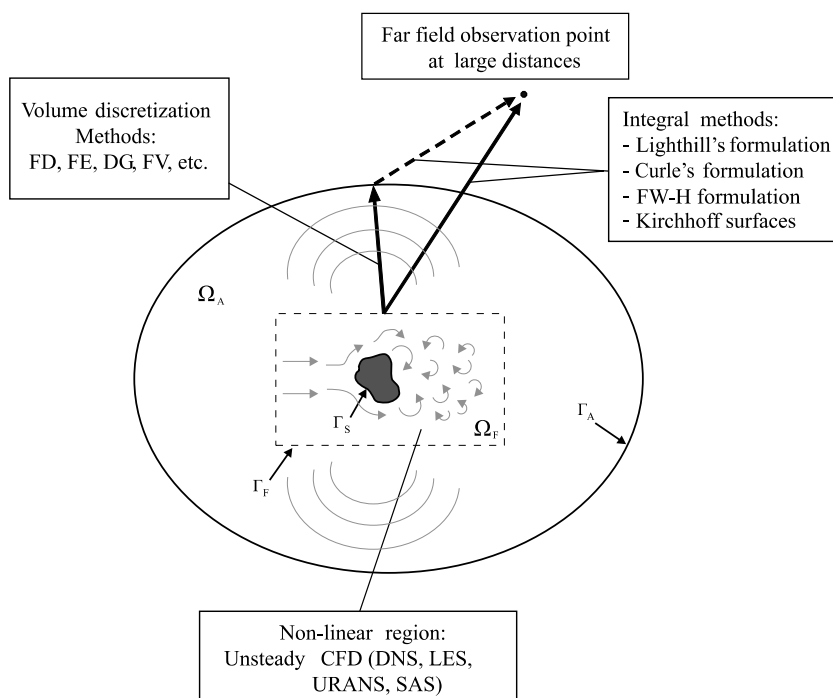


Fig. 4.1 Schematic depicting some of the possible strategies when using an aeroacoustic hybrid approach.

lation (DES) [44] which allows the turbulence model to transition from an uRANS (unsteady Reynolds Averaged Navier Stokes) method for attached boundary layers to a LES in separated regions. Another recently developed approach is the Scale-Adaptive Simulation method (SAS) [38] which instead of producing the large-scale unsteadiness, typically observed in uRANS simulations, it adjusts to the already resolved scales in a dynamic way and allows the development of a turbulent spectrum in the detached regions. It therefore behaves in a way much similar to a DES model, but without the explicit grid dependence in the RANS regime [38]. A thorough review of the current ongoing research in CFD methods used for CAA simulations can be found in [53].

Among the group of hybrid approaches, integral methods remain widely used in CAA for solving open domain problems in large acoustic domains like airframe noise, landing gear noise simulation, fan (turbines) noise, rotor noise, etc. One reason which motivates the use of integral formulations in such applications is that, in general, their acoustic sources can be considered to be compact and only an extension of the acoustic solution at a few points in the far field is desired. Therefore, in such cases, integral methods as Lighthill's acoustic analogy, see, e.g., [23, 31], Curle's formulation, see, e.g., [10], Ffwoes Williams and Hawkins formulation,

see, e.g., [6, 10, 19], Kirchhoff method, see, e.g., [6, 17] or extension thereof, see, e.g., [11, 18, 35, 36] are computationally less expensive than volume discretization methods where a whole discretization of the acoustic domain is required. Integral approaches are derived by using free field Green's functions, being the Ffwoos Williams and Hawkings formulation the most widely used among these. The reason is that it is generalized to account for noise generation effects due to moving surfaces immersed in a turbulent flow.

On the other hand, for confined aeroacoustic problems, where non-compact solid boundaries are present, or if structural/acoustic effects are considered, it is more appropriate to use a volume discretization method to account for the interactions between the solid surfaces and the flow-induced noise directly in the acoustic simulation. In such cases, integral formulations would require a priori knowledge of a hard-wall Green's function that is not known for complex geometries [42]. Furthermore, volume discretization methods are capable to include the effects of wave propagation in non-uniform background flows.

Among the volume discretization methods used in CAA we find finite differences (FD), discontinuous Galerkin (DG) or finite volume (FV) schemes, generally employed to solve aeroacoustic formulations based on Linearized Euler Equations, see, e.g., [5, 27, 37, 50], or systems of equations alike: Acoustic Perturbation Equation, see [16], Linearized Perturbed Compressible Equation, see [49]. Additionally, we find the Finite Element (FE) method used to solve the variational formulation of Lighthill's acoustic analogy [3, 43]. Figure 4.1 also depicts the general configuration when using these methods. Herewith, Ω_F denotes the region where the flow field is firstly computed and where the acoustic sources are interpolated from the fluid simulation to the acoustic computation. The acoustic propagation region is given by $\Omega_F \cup \Omega_A$ where the acoustic field is computed in a second step, by solving the inhomogeneous wave equation or a corresponding set of equations depending on the CAA methodology followed. Since interior methods require the whole discretization of the propagation domain, usually they are used to compute the radiated sound until an intermediate region in the far field (i.e. until Γ_A in Figure 4.1), before moving to an integral formulation in which the acoustic solution from the volume discretization method at the interface is used as input for computing pressure levels at further points. Such a combined scheme has been presented, e.g., by Manoha et al. [37] solving the Euler equations for the intermediate inhomogeneous flow region and a 3D Kirchhoff method for the far field noise. For a more detailed discussion on the different CAA methodologies we refer to [15].

4.2 Hybrid Approach Using Lighthill's Acoustic Analogy

4.2.1 Lighthill's Acoustic Analogy

Many hybrid approaches employed in CAA, including the one presented here, are based on the inhomogeneous wave equation as derived by Lighthill in [31]. This formulation allows the calculation of the acoustic radiation from relatively small

regions of turbulent flow embedded in a homogeneous fluid. For the derivation of the inhomogeneous wave equation Lighthill starts from the continuity and momentum equations which, by using the summation convention, can be written as [23, 31]

$$\frac{\partial \rho}{\partial t} + \frac{\partial \rho u_j}{\partial x_j} = 0 \quad (4.1)$$

$$\rho \frac{\partial u_i}{\partial t} + u_j \frac{\partial \rho u_i}{\partial x_j} = - \frac{\partial p}{\partial x_i} - \frac{\partial \tau_{ij}}{\partial x_j}. \quad (4.2)$$

In (4.1) and (4.2) ρ denotes the density of the fluid, v_i the i -th component of the flow velocity vector \mathbf{v} , p the overall pressure and τ_{ij} the (i, j) th component of the viscous stress tensor. For a Stokesian gas it can be expressed in terms of the velocity gradients by

$$\tau_{ij} = -\mu \left(\frac{\partial u_i}{\partial x_j} + \frac{\partial u_j}{\partial x_i} - \frac{2}{3} \mu \delta_{ij} \frac{\partial u_k}{\partial x_k} \right), \quad (4.3)$$

where μ is the viscosity of the fluid and δ_{ij} the Kronecker delta.

Multiplying the continuity Equation (4.1) by u_i , adding the result to the momentum equation, and combining terms yields

$$\frac{\partial \rho u_i}{\partial t} = - \frac{\partial}{\partial x_j} (\rho u_i u_j + \delta_{ij} p + \tau_{ij}), \quad (4.4)$$

which after adding and subtracting the term $c_0^2 \partial \rho / \partial x_i$ (c_0 denotes the speed of sound), becomes

$$\frac{\partial \rho u_i}{\partial t} + c_0^2 \frac{\partial \rho}{\partial x_i} = - \frac{\partial T_{ij}}{\partial x_j}. \quad (4.5)$$

In (4.5), T_{ij} denotes Lighthill's stress tensor given as

$$T_{ij} = \rho u_i u_j + \delta_{ij} [(p - p_0) - c_0^2 (\rho - \rho_0)] + \tau_{ij} \quad (4.6)$$

with ρ_0 and p_0 the atmospheric values of density and pressure respectively. Now it is possible to differentiate (4.1) with respect to t , take the divergence of (4.5), and subtract the results to obtain Lighthill's inhomogeneous wave equation solving for the acoustic density ρ' [23, 31]

$$\frac{\partial^2 \rho'}{\partial t^2} - c_0^2 \frac{\partial^2 \rho'}{\partial x_i^2} = \frac{\partial^2 T_{ij}}{\partial x_i \partial x_j}. \quad (4.7)$$

An important aspect in Lighthill's acoustic analogy, in order to be able to compute the noise radiation, is the assumption that Lighthill's stress tensor is a known source term or at least can be evaluated to a certain degree of approximation. Additionally, this source term is assumed to vanish outside the turbulent region. Indeed, for a turbulent flow embedded in a uniform atmosphere at rest, Lighthill's stress tensor $T_{ij} = \rho u_i u_j + \delta_{ij} [(p - p_0) - c_0^2 (\rho - \rho_0)] + \tau_{ij}$ can be neglected outside the turbulent region itself. In this outer region the velocity u_i consists only of the

small motions characteristics of sound. Furthermore, this velocity appears quadratically in the calculation of the tensor as $\rho u_i u_j$. Moreover, the effects of viscosity and heat conduction are expected to cause only a slow damping due to the conversion of acoustic energy into heat and to have a significant effect only over very large distances. Therefore, it should be possible to neglect τ_{ij} entirely [23].

The term $(p - p_0) - c_0^2(\rho - \rho_0)$, becomes of importance only for anisotropic media, when the Mach number in the acoustic domain is significantly different from the one in the fluid domain. Otherwise, for isentropic flows in which $(p - p_0)/p_0$ and $(\rho - \rho_0)/\rho_0$ are very small, the isentropic relation

$$(p - p_0) = c_0^2(\rho - \rho_0) \quad (4.8)$$

can be assumed. Therefore, the resulting approximate of Lighthill's tensor is given by

$$T_{ij} \approx \rho u_i u_j. \quad (4.9)$$

Lighthill pointed out in [31], that the resulting approximate tensor could also be found from an approach which makes approximations in the equations of motion right from the beginning of the derivation of Lighthill's inhomogeneous equation, but that approximations at that early stage could introduce dipole or monopole sources whose contribution to the radiated sound might be relatively large.

The explicit separation of propagation and generation as derived by Lighthill has arised many discussions ever since, which have motivated the derivation of improved acoustic analogy formulations. A difficulty of Lighthill's equation is the interpretation of the source term where mean flow effects on the wave propagation are included [46]. In such cases, a compressible velocity field is required for the evaluation of the source term. In order to obtain a formulation to describe the noise propagation in a transversally sheared mean flow, Lilley [32,33] proposed a third-order wave operator. The mean flow and any refraction it causes are explicitly considered in this wave operator. However, this formulation does not provide any obvious simplification of the sources, still leaving complex combinations of terms which must be modeled in making predictions. Since there is no clear simplification that comes about by including more propagation physics into the wave operator, it can therefore be argued that the Lighthill approach is no worse off than such a more sophisticated approach. Since acoustic analogies are exact, an accurate representation of the source in the original Lighthill's analogy provides the correct sound despite the multiple physical effects grouped into it. Since different acoustic analogies require different source models, it is difficult to make clear direct comparisons between them and thus, difficult to judge if one is preferable to others [22].

4.2.2 Weak Formulation

The weak formulation of the initial/boundary-value problem can be derived applying the method of weighted residuals and by making use of a usual space of functions

$$\vartheta = \{u(\cdot, t) \mid u(\mathbf{x}, t) \in H^1, \mathbf{x} \in \Omega\}, \quad (4.10)$$

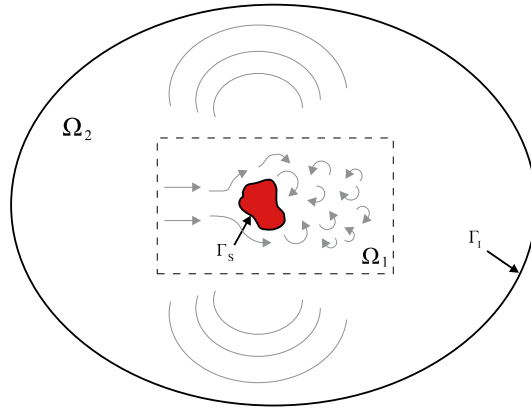


Fig. 4.2 General setup for a flow-induced noise problem

where H^1 denotes the Sobolev space defined as, see e.g. [1],

$$H^1 = \{u \in L^2 | \partial u / \partial x_i \in L^2\} \quad (4.11)$$

and L^2 the space of square integrable functions. After multiplication by an appropriate test function w from the space of functions given in (4.10) and integration over the whole domain Ω , see Figure 4.2, the problem can be formulated in the integral form as (using now the acoustic pressure p' as the unknown physical quantity)

$$\begin{aligned} \int_{\Omega} \frac{1}{c_0^2} \frac{\partial^2 p'}{\partial t^2} w \, d\Omega - \int_{\Omega} \frac{\partial^2 p'}{\partial x_i^2} w \, d\Omega &= \int_{\Omega} \frac{\partial^2 T_{ij}}{\partial x_i \partial x_j} w \, d\Omega \\ \int_{\Omega} p'(\mathbf{x}, 0) w \, d\Omega &= \int_{\Omega} p'_0 w \, d\Omega \\ \int_{\Omega} \frac{\partial p'}{\partial t}(\mathbf{x}, 0) w \, d\Omega &= \int_{\Omega} \dot{p}'_0 w \, d\Omega \quad \forall w \in H^1. \end{aligned} \quad (4.12)$$

Now, we apply Green's integral theorem in the first equation in (4.12) to the second spatial derivative of p' as well as to the acoustic source term containing T_{ij} . This operation results in the following relations

$$\int_{\Omega} w \frac{\partial^2 p'}{\partial x_i^2} \, d\Omega = \int_{\Gamma_S \cup \Gamma_1} w \frac{\partial p'}{\partial \mathbf{n}} \, d\Gamma - \int_{\Omega} \frac{\partial w}{\partial x_i} \frac{\partial p'}{\partial x_i} \, d\Omega \quad (4.13)$$

$$\int_{\Omega} w \frac{\partial^2 T_{ij}}{\partial x_i \partial x_j} \, d\Omega = \int_{\Gamma_S} w \frac{\partial T_{ij}}{\partial x_j} n_i \, d\Gamma - \int_{\Omega} \frac{\partial w}{\partial x_i} \frac{\partial T_{ij}}{\partial x_j} \, d\Omega. \quad (4.14)$$

Herewith, it is important to emphasize, that the boundary integral in (4.14) is just over the surface Γ_S of any solid/elastic body since we assume T_{ij} to be zero at the

limits the computational domain Γ_1 , whereas in (4.13) we have to integrate over Γ_S as well as over Γ_1 , see Figure 4.2. By using the momentum conservation law and assuming a solid body, e.g. $u_i n_i = 0$ where \mathbf{u} denotes the velocity of the body, we can express the surface integral in (4.14) by

$$\int_{\Gamma_S} w \frac{\partial T_{ij}}{\partial x_j} n_i d\Gamma = - \int_{\Gamma_S} w \frac{\partial p'}{\partial \mathbf{n}} d\Gamma. \quad (4.15)$$

Therewith, we can combine the two surface integrals to a single one just performed over the outer boundary Γ_1 . This remaining surface integral corresponds to the natural boundary condition associated with the weak formulation and will be employed later for applying absorbing boundary conditions. Finally, we arrive at the weak form of (4.7): Find $p' \in H^1$ such that

$$\begin{aligned} \int_{\Omega} \frac{1}{c_0^2} w \frac{\partial^2 p'}{\partial t^2} d\Omega + \int_{\Omega} \frac{\partial w}{\partial x_i} \frac{\partial p'}{\partial x_i} d\Omega - \int_{\Gamma_1} w \frac{\partial p'}{\partial \mathbf{n}} d\Gamma \\ = - \int_{\Omega} \frac{\partial w}{\partial x_i} \frac{\partial T_{ij}}{\partial x_j} d\Omega \end{aligned} \quad (4.16)$$

is fulfilled for all $w \in H^1$. For the flow induced noise computation, we will consider two different methods for treating the outer boundary Γ_1 . In the transient case, we apply first order absorbing boundary conditions [14], which results in the following simple substitution

$$\frac{\partial p'}{\partial \mathbf{n}} = \frac{1}{c_0} \frac{\partial p'}{\partial t}. \quad (4.17)$$

However, this boundary condition is just optimal for acoustic waves impinging orthogonal onto the boundary Γ_1 , whereas for all other waves numerical reflections occur. Therewith, a limitation of the computational domain within the acoustic near field will result in worse results. For the harmonic case, we will apply a recently developed Perfectly Matched Layer (PML) technique [29]. For this method, we enclose our computational domain by an additional damping layer, see Figure 4.3, in which the acoustic waves are damped and where at the interface between the propagation and damping region no reflections occur. Therewith, with such a PML technique, we can limit the computational domain even in the acoustic near field.

4.2.3 Spatial Discretization

The semidiscrete Galerkin formulation is obtained from the weak formulation of the equation after discretization of the domain with finite elements. The entire domain, $\Omega = \Omega_1 \cup \Omega_2$, is discretized by an approximate decomposition \sum_h of Ω into \mathbb{R}^2 or \mathbb{R}^3 finite elements. From our previously defined space \mathcal{V} , we choose a finite dimensional space $\mathcal{V}_h \subset \mathcal{V}$. We can now write a variational equation of the form of (4.16) in terms of $p'_h \in \mathcal{V}_h$, using the nabla differential operator for better readability and neglecting the term on the boundary Γ_1

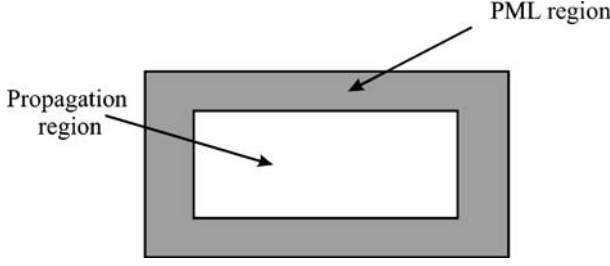


Fig. 4.3 Computational setup: propagation region surrounded by a PML-region.

$$\int_{\Omega_h} \frac{1}{c_0^2} \ddot{p}'_h w_h d\Omega + \int_{\Omega_h} \nabla p'_h \cdot \nabla w_h d\Omega = - \int_{\Omega_h} (\nabla \cdot T_{ij}) \cdot \nabla w_h d\Omega. \quad (4.18)$$

Using standard nodal finite elements, we can approximate the continuous pressure perturbation p' as well as the test function w in terms of the interpolation functions as⁵

$$p' \approx p'_h(t) = \sum_{i=1}^{n_{eq}} N_i(\mathbf{x}) p'_i(t) \quad (4.19)$$

$$w \approx w_h = \sum_{i=1}^{n_{eq}} N_i(\mathbf{x}) c_i, \quad (4.20)$$

where $N_i(\mathbf{x})$ denote appropriate interpolation functions and c_i the corresponding weights. From (4.18), we can now write the semidiscrete Galerkin formulation in matrix form as

$$\mathbf{M} \ddot{\mathbf{p}}'(t) + \mathbf{K} \mathbf{p}'(t) = \mathbf{f}, \quad (4.21)$$

where the matrices \mathbf{M} and \mathbf{K} are computed as follows

$$\mathbf{M} = [M_{ij}] \quad M_{ij} = \int_{\Omega} \frac{1}{c_0^2} N_i N_j d\Omega \quad (4.22)$$

$$\mathbf{K} = [K_{ij}] \quad K_{ij} = \int_{\Omega} \left(\frac{\partial N_i}{\partial x_1} \frac{\partial N_j}{\partial x_1} + \frac{\partial N_i}{\partial x_2} \frac{\partial N_j}{\partial x_2} + \frac{\partial N_i}{\partial x_3} \frac{\partial N_j}{\partial x_3} \right) d\Omega. \quad (4.23)$$

Finally, the right-hand-side vector including the acoustic sources reads

$$\mathbf{f} = \{f_i\}$$

$$f_i = - \int_{\Omega} \left(\frac{\partial N_i}{\partial x_1}, \frac{\partial N_i}{\partial x_2}, \frac{\partial N_i}{\partial x_3} \right) \cdot \frac{\partial T_{ij}}{\partial x_j} d\Omega. \quad (4.24)$$

⁵The evaluation of the source terms using the same kind of interpolation functions is considered in Section 4.2.6, while at this point they are treated as given continuous values sampled at the finite element nodes.

4.2.4 Time Discretization

In order to discretize our problem in the time domain, the Newmark scheme is typically applied, see e.g. [28]. Let us start from the semidiscrete Galerkin formulation in matrix form

$$\mathbf{M}\ddot{\mathbf{p}}'_{n+1} + \mathbf{K}\mathbf{p}'_{n+1} = \mathbf{f}_{n+1} \quad (4.25)$$

with \mathbf{M} the mass matrix, \mathbf{K} the stiffness matrix, \mathbf{f} the right hand side, \mathbf{p}' the vector of unknowns at the finite element nodes and $\ddot{\mathbf{p}}'$ its second derivative with respect to time. For hyperbolic partial differential equations the *Newmark* scheme is generally used. Therewith, we have, see e.g. [28],

$$\mathbf{p}'_{n+1} = \mathbf{p}'_n + \Delta t \dot{\mathbf{p}}'_n + \frac{\Delta t^2}{2} [(1 - 2\beta_H)\ddot{\mathbf{p}}'_n + 2\beta_H\ddot{\mathbf{p}}'_{n+1}] \quad (4.26)$$

$$\dot{\mathbf{p}}'_{n+1} = \dot{\mathbf{p}}'_n + \Delta t [(1 - \gamma_H)\ddot{\mathbf{p}}'_n + \gamma_H\ddot{\mathbf{p}}'_{n+1}] \quad (4.27)$$

In (4.26)–(4.27) n denotes the time step counter, Δt the time step value and β_H , γ_H the integration parameters. Substituting \mathbf{p}'_{n+1} and $\dot{\mathbf{p}}'_{n+1}$ according to (4.26) and (4.27) in (4.25) leads to the following algebraic system of equations

$$\mathbf{M}^* \ddot{\mathbf{p}}'_{n+1} = \mathbf{f}_{n+1} - \mathbf{K} \left[\mathbf{p}'_n + \gamma_H \Delta t \dot{\mathbf{p}}'_n + \frac{\Delta t^2}{2} (1 - 2\beta_H) \ddot{\mathbf{p}}'_n \right] \quad (4.28)$$

$$\mathbf{M}^* = \mathbf{M} + \beta_H \Delta t^2 \mathbf{K} \quad (4.29)$$

Writing the solution process for one time step as a *predictor–corrector* algorithm we arrive at the following formulations, also known as the *effective mass formulation*.

- Perform predictor step:

$$\tilde{\mathbf{p}}' = \mathbf{p}'_n + \Delta t \dot{\mathbf{p}}'_n + (1 - 2\beta_H) \frac{\Delta t^2}{2} \ddot{\mathbf{p}}'_n \quad (4.30)$$

$$\tilde{\dot{\mathbf{p}}}' = \dot{\mathbf{p}}'_n + \Delta t (1 - \gamma_H) \ddot{\mathbf{p}}'_n \quad (4.31)$$

- Solve algebraic system of equations:

$$\mathbf{M}^* \ddot{\tilde{\mathbf{p}}}'_{n+1} = \mathbf{f}_{n+1} - \mathbf{K} \tilde{\mathbf{p}}' \quad (4.32)$$

$$\mathbf{M}^* = \mathbf{M} + \beta \Delta t^2 \mathbf{K} \quad (4.33)$$

- Perform corrector step:

$$\mathbf{p}'_{n+1} = \tilde{\mathbf{p}}' + \beta_H \Delta t^2 \ddot{\tilde{\mathbf{p}}}'_{n+1} \quad (4.34)$$

$$\dot{\mathbf{p}}'_{n+1} = \tilde{\dot{\mathbf{p}}}' + \gamma_H \Delta t \ddot{\tilde{\mathbf{p}}}'_{n+1} \quad (4.35)$$

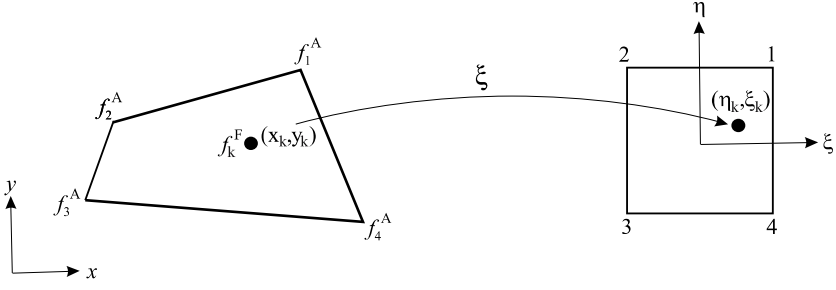


Fig. 4.4 Global to local mapping for conservative interpolation

4.2.5 Harmonic Formulation

By applying a harmonic analysis, it is possible to compute the sound radiation for specific frequency components present in the acoustic sources. In this way, we obtain the complex acoustic pressure present at each node in the numerical domain. For deriving the harmonic counterpart we apply a Fourier–transformation to the semidiscrete Galerkin formulation (4.25), obtaining the following complex algebraic system of equations

$$(-\omega^2 \mathbf{M} + \mathbf{K}) \hat{\mathbf{p}} = \hat{\mathbf{f}}, \quad (4.36)$$

where the source term $\hat{\mathbf{f}}$ represents the complex nodal acoustic sources, which are obtained by applying a Fourier transformation to the dataset of transient nodal sources interpolated from the fluid computation.

4.2.6 Coupling Scheme

A crucial point is the transformation of the acoustic sources from the computed flow data to the acoustic grid. In order to preserve the acoustic energy, we perform an integration over the source volume (corresponds to the computational flow region) within the FE formulation and project the results to the nodes of the fine flow grid, which has to be interpolated to the coarser acoustic grid. Therewith, our interpolation has to be conservative in order to preserve the total acoustic energy. As illustrated in Figure 4.4, we have to find for each nodal source f_k^F in which finite element of the acoustic grid it is located. Then, we compute from the global position (x_k, y_k) its position (ξ_k, η_k) in the reference element. This is in the general case a non–linear mapping and is solved by a Newton scheme. Now, with this data we can perform a bilinear interpolation and add the contribution of f_k^F to the nodes of the acoustic grid by using the standard finite element basis functions N_i

$$f_i^A = N_i(\xi_k, \eta_k) f_k^F.$$

Therewith, by this procedure the interpolation preserves the overall sum of the acoustic sources.

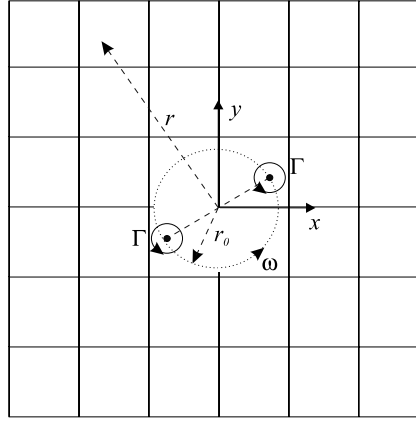


Fig. 4.5 Schematic diagram of corotating vortices.

4.3 Validation of the Computational Scheme

For validation, we consider the acoustic far field caused by an incompressible, purely unsteady vortical flow. The inhomogeneous wave equation is forced with the acoustic sources obtained from the analytical hydrodynamic field induced by a co-rotating vortex pair. CAA investigations using these types of flow fields are a practical way to validate the simulation of flow-induced noise problems [12, 13, 16, 30, 34]. The resulting acoustic field represents the basic acoustic field generated by turbulent shear flows, jet flows, edge tones, etc. [30].

4.3.1 Theoretical Approach

The acoustic sources in the flow region are computed from the hydrodynamic quantities of the flow field induced by a spinning vortex pair. This corotating vortex pair consists of two point vortices which are separated by a fixed distance of $2r_0$ with circulation intensity Γ . The schematic of the corotating vortices is presented in Figure 4.5. These vortices rotate around each other with a period $T = 8\pi^2 r_0^2 / \Gamma$. Each vortex induces on the other a velocity $v_\theta = \Gamma / (4\pi r_0)$. The configuration results in a rotating speed $\omega = \Gamma / (4\pi r_0^2)$, and rotating Mach number $Ma_r = v_\theta / c_0 = \Gamma / (4\pi r_0 c_0) = 2\pi r_0 / T c_0$. The rotating noncircular streamlines are directly associated with the hydrodynamic field of the rotating quadrupole [30]. The incompressible, inviscid flow can be determined numerically by the evaluation of a complex potential function $\Phi(z, t)$ [13, 16, 20]

$$\Phi(z, t) = \frac{\Gamma}{2\pi i} \ln(z - b) + \frac{\Gamma}{2\pi i} \ln(z + b) = \frac{\Gamma}{2\pi i} \ln z^2 \left(1 - \frac{b^2}{z^2}\right), \quad (4.37)$$

where $z = r e^{i\theta}$ and $b = r_0 e^{i\omega t}$. For $|z/b| \gg 1$, (4.37) can be approximated by

$$\Phi(z, t) \approx \frac{\Gamma}{\pi i} \ln z - \frac{\Gamma}{2\pi i} \left(\frac{b}{z} \right)^2 = \Phi_0 + \Phi_1. \quad (4.38)$$

The first term on the right hand side of (4.38) represents a steady vortical flow, whereas the second term represents the fluctuation with the fundamental frequency due to the vortex motion [30].

From (4.37) it is then possible to derive the expressions representing the hydrodynamic quantities required to compute the acoustic sources when following the acoustic analogy approach. The hydrodynamic velocity is obtained by differentiating (4.37) with respect to z

$$u_x - iu_y = \frac{\partial \Phi(z, t)}{\partial z} = \frac{\Gamma}{i\pi} \frac{z}{z^2 - b^2}. \quad (4.39)$$

In the acoustic computation a linear propagation is assumed outside the fluid region, governed by the homogeneous acoustic wave equation.

For comparison with the numerical results, the analytical solution of the acoustic pressure fluctuations from the corotating vortex pair, obtained with the matched asymptotic expansion (MAE) method, is given by [41]

$$p' = \frac{\rho_0 \Gamma^4}{64\pi^3 r_0^4 c_0^2} [J_2(kr) \cos(\Psi) - Y_2(kr) \sin(\Psi)], \quad (4.40)$$

where $k = 2\omega/c_0$, $J_2(kr)$, $Y_2(kr)$ are the second-order Bessel functions of the first and second kind and $\Psi = 2(\omega t - \theta)$. An equivalent expression for this quadrupole-like solution has also been derived by Mitchell et al. [39] starting from the vortex sound theory proposed by Möhring [40].

4.3.2 Numerical Investigation

In the computations, we have evaluated the flow field induced by the spinning vortex pair in a numerical region with dimensions $200 \text{ m} \times 200 \text{ m}$. This region corresponds to the region, where the acoustic nodal sources for the inhomogeneous wave equation are computed. The acoustic propagation is computed in a larger numerical domain with dimensions $400 \text{ m} \times 400 \text{ m}$, as the one depicted in Figure 4.6 where the inner square domain corresponds to the source region. For evaluating the complex potential function the spinning radius is chosen to be $r_0 = 1 \text{ m}$, the circulation intensity $\Gamma = 1.00531 \text{ m}^2/\text{s}$ and the speed of sound $c_0 = 1 \text{ m/s}$. This results in a wave length $\lambda \approx 39 \text{ m}$ and a rotating Mach number $Ma_r = 0.0796$.

In Lighthill's acoustic analogy we require the velocity vector field to compute the velocity gradients contained in the acoustic source term. This aspect makes it necessary to evaluate the fluid field using a much finer resolution than that of the acoustic field, so that the velocity gradients can be computed accurately. Therefore, we employ our coupling approach as follows. The first step consists in evaluating analytically the velocity field and then numerically the right hand side of our FE formulation, see (4.24), on a fine fluid grid. Secondly, after interpolation of the acoustic

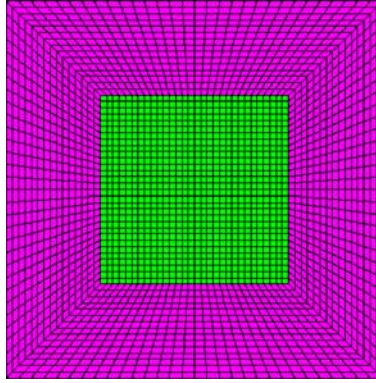


Fig. 4.6 Configuration of numerical domain as used for the computation of the acoustic propagation induced by the corotating vortex pair.

nodal loads from the fine fluid grid to the coarser acoustic grid, we solve the inhomogeneous wave equation to obtain the acoustic solution.

An additional issue for the computation is the singularity of the velocity field at the point vortices. Since the acoustic contribution of the region near the point vortices is important for the final acoustic field, a cut-off of the sources at these region, as proposed in [13], does not produce good results. Therefore, the application of a vortex core model, as proposed in [16,30,45,47], is required to obtain the desingularized tangential velocity field around these points. A desingularized kernel following the Scully model [4,48] and presented in [45,47] is applied at each point vortex for radii $r_{\text{vortex}} < 0.15$ m. Within these regions the expressions for the velocity components are given by

$$u_x = -\frac{\Gamma}{2\pi} \frac{y}{r_{\text{core}} + x^2 + y^2}; u_y = \frac{\Gamma}{2\pi} \frac{x}{r_{\text{core}} + x^2 + y^2}, \quad (4.41)$$

where the coordinates (x, y) are taken with respect to each vortex and r_{core} corresponds to the vortex core radius, which is the distance from the point vortex where the maximum tangential velocity values occur. For the computations, a value $r_{\text{core}} = 0.10$ m has been chosen.

For the computations presented here we have used a grid size h_f , which corresponds to $r_{\text{core}}/h_f = 5$ in a region around the corotating vortices with dimensions $6 \text{ m} \times 6 \text{ m}$. Outside this area the grid is coarsened in radial directions. For the transient acoustic computation, the grid is correspondingly coarsened in the coupled region and it extends 500 m in all directions to avoid the effects of boundary reflections on the solution. In this case the element size for the acoustic grid in the region next to the spinning vortices is chosen to be $h_a = 0.1$ m which corresponds to $h_a/h_f = 5$. Since the applied vortex core model is an approximation of the velocity field near the point vortices, the evaluation of the velocity gradients at these regions still remains very sensible and numerical oscillations are still present even with a very fine

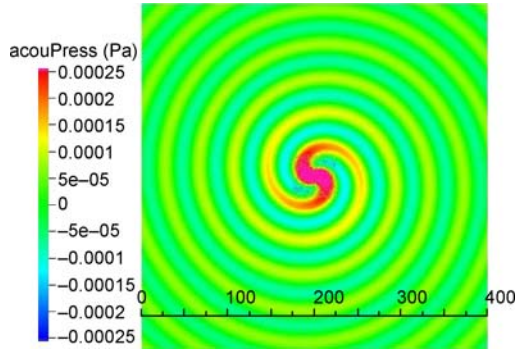


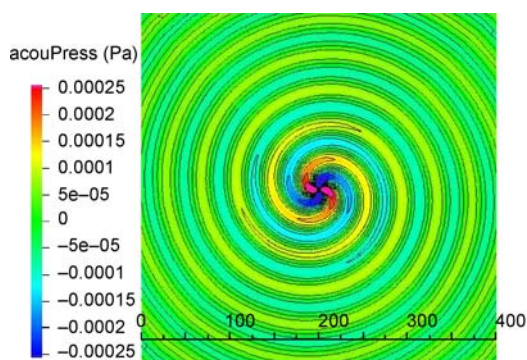
Fig. 4.7 Contour plot of acoustic pressure field at time $t = 413$ s computed using a temporal ramping of the initial acoustic sources. Distance scale in meters.

discretization. Therefore, transient results of the acoustic pressure field show some numerical noise as can be observed from the contour plot of the acoustic field at time $t = 413$ s presented in Figure 4.7, where a time step size $\Delta t = 0.5$ s was used.

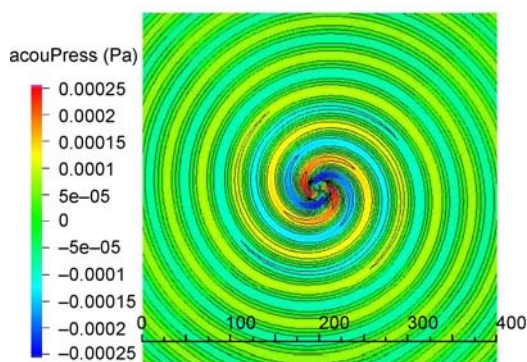
To completely suppress transient numerical noise in the acoustic pressure field, the interpolated transient acoustic sources are transformed to the frequency domain and a harmonic analysis is carried out for the main frequency component of the problem, $f = 1/T \approx 0.026$ Hz. A comparison of the acoustic field from the numerical results with the analytical solution is presented in Figure 4.8. Good agreement in both the spiral pattern as well as in amplitudes is found in the far field acoustic pressure except at the center of the computational domain, where the evaluation of the analytical solution resulted in a non-physical behavior. Figure 4.9 compares the decay of the acoustic pressure along the positive x -axis between the transient result, the harmonic result and the analytical solution. Apart from the spurious noise in the transient simulation at distances $x < 40$ m within the source region, numerical decays present good correspondence with the far-field analytical values.

4.4 Flow-induced Noise from 3D Wall Mounted Cylinders

We investigate the flow-induced noise from wall-mounted cylinders using two different geometry profiles, a standard square cylinder geometry and a cylinder with elliptic shape in the downstream direction. The general set-up for the coupled simulation is depicted in Figure 4.10. Ω_1 denotes the region where the flow field is computed and where the acoustic sources are interpolated from the fluid grid to the acoustic grid. The region encompassing Ω_1 and Ω_2 corresponds to the region where the acoustic propagation is computed. Two different geometry profiles evaluated in the numerical investigations are depicted in Figures 4.11 and 4.12. Based on the crossflow side length of $D = 20$ mm, the Reynolds number Re for both fluid calculations results in about 13.000.



(a) Acoustic pressure field at frequency $f = 0.026$ Hz, from hybrid computation following Lighthill's acoustic analogy



(b) Analytical acoustic pressure field obtained using MAE

Fig. 4.8 Comparison of sound pressure field obtained numerically using Lighthill's acoustic analogy with analytical solution obtained using MAE method. Distance scale in meters.

4.4.1 Flow Computations

The flow-induced noise investigations for the square cylinder and the square cylinder with elliptical afterbody are based on fluid results computed with ANSYS-CFX.⁶ The numerical domain is described in Figure 4.13, where $D = 20$ mm. For both configuration a block profile inflow velocity of $u_x = 10$ m/s have been applied. The boundary conditions used in the fluid computation with respect to the configuration from Figure 4.13 are described in Table 4.1. For the simulation of the flow a turbulence modeling approach based on SAS (Scale Adaptive Simulation) was employed. The SAS approach allows to use coarser grids than those used in standard LES (Large Eddy Simulation) computations. For both configurations, the compu-

⁶See www.ansys.com/cfx, ANSYS-CFX software

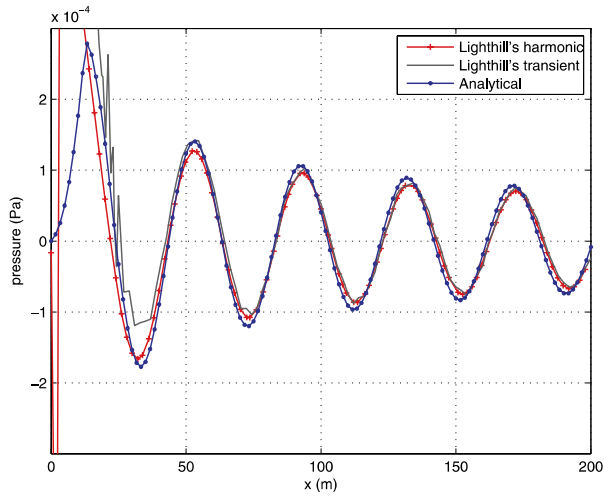


Fig. 4.9 Decay of the acoustic pressure values along the x-axis

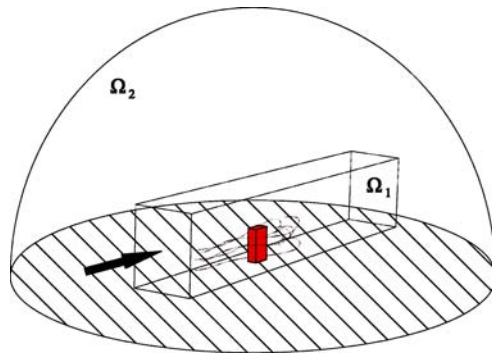


Fig. 4.10 Schematic representation of the hybrid domain as used for the 3D computations.

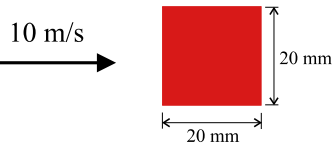


Fig. 4.11 Square cylinder profile

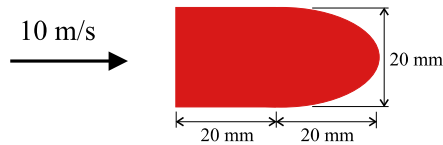


Fig. 4.12 Square cylinder with elliptical afterbody

tational grid consists of about 1.1 million cells, and for time step size a value of $\Delta t_f = 20 \mu s$ has been chosen.

Figure 4.14 shows the obtained transient flow fields at one instantaneous time step. The visualization displays isosurfaces of $\Omega^2 - S^2 = 100000 s^{-2}$ colored with the eddy viscosity, where Ω representing here the vorticity and S the strain rate.

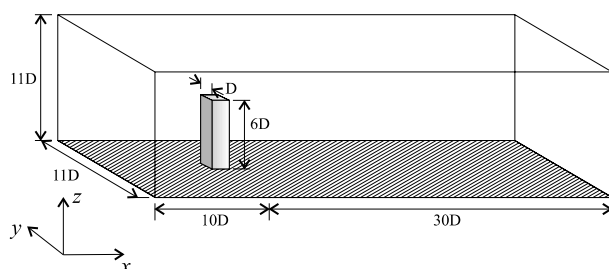


Fig. 4.13 Numerical domain used for fluid computations ($D = 20$ mm)

Table 4.1 Boundary conditions used for fluid computations

| Position | Boundary Condition |
|------------------|-----------------------------|
| $X = 0$ | block inlet profile, 10 m/s |
| $X = 40D$ | convective exit boundary |
| $Z = 11D$ | symmetry boundary condition |
| $Y = 0, Y = 11D$ | symmetry boundary condition |
| wall | no slip boundary condition |

4.4.2 Acoustic Computations

Square Wall-Mounted Cylinder

For the square cylinder profile, acoustic simulations have been performed in time and frequency domain, using the results from the fluid computations presented in the previous section. Directly coupled transient computations were performed, using an acoustic grid with radius $r = 3$ m, consisting of 3.683.670 tetrahedral elements with quadratic basis functions which resulted in 4.986.115 finite element nodes. The coupled region has been discretized with 135.173 nodes. Since the conservative interpolation scheme using MpCCI⁷ is restricted to volume interpolation of linear 3D elements, the acoustic sources have been interpolated on the 17.925 corner (linear) nodes of the quadratic tetrahedral elements.

Figure 4.15 presents the numerical grid in which first order absorbing boundary conditions have been applied on the hemisphere boundary using 51.896 triangular surface elements. A closer view of the coupled region depicting the edges of the tetrahedral elements on the bottom plane and on the cylinder surface is shown in Figure 4.16. The isosurfaces of the near-field acoustic pressure obtained from the flow computations are displayed in Figure 4.17. The time step size for the 3D acoustic computation was chosen to be $\Delta t_a = 10 \cdot \Delta t_f = 200 \mu\text{s}$. For these low frequency tonal noise problems, further quantitative analysis of 3D transient results is restricted due to the large wavelength expected for these specific problems ($\lambda \approx 6.2$ m for

⁷See: <http://www.mpcci.org>, Mesh-based parallel Code Coupling Interface – MpCCI 3.0 Specifications, Fraunhofer Institute, Germany

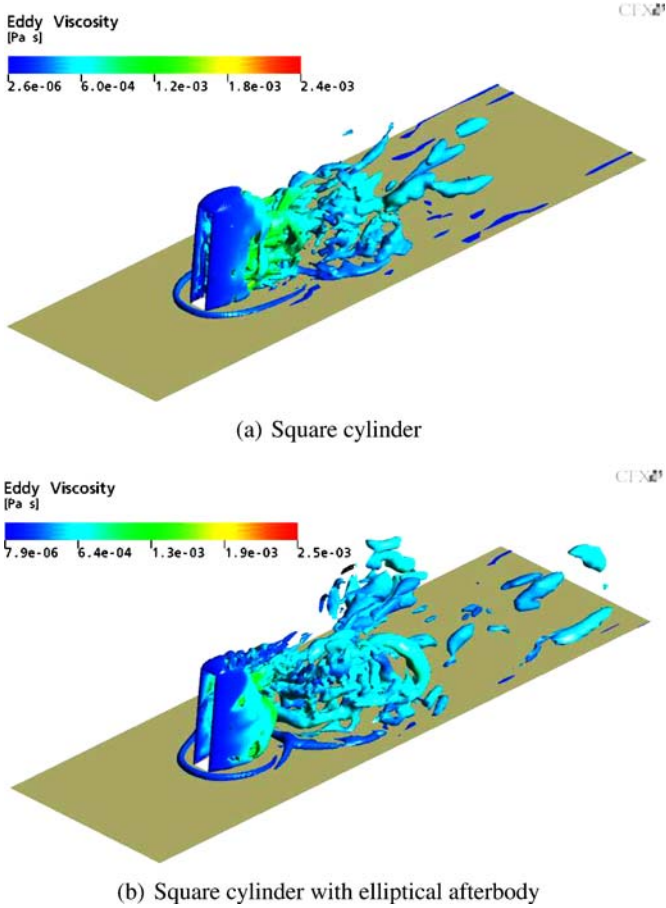


Fig. 4.14 Instantaneous visualization of transient flow field.

$f = 55 \text{ Hz}$) and the high computational cost due to the very large number of elements required to cover higher frequency signals present in the acoustic sources. Therefore, for more practical analysis of this type of aeolian tone problems, we perform harmonic analyses for the main frequency components. The main advantage of computing in frequency domain is that the acoustic field is solved only for relevant frequency components, avoiding in this way high frequency transient numerical noise. Furthermore, in the 3D computations we can also use our enhanced PML method [29], which allows smaller acoustic domains producing almost no spurious reflections. This aspect significantly reduces the computational time.

In Figure 4.18 the configuration of the simulation domain for the harmonic computation showing the monitoring points used for directivity analysis is presented. Due to the rectangular configuration of the acoustic domain, the discretization could be performed using hexahedron elements with quadratic basis functions, which in-

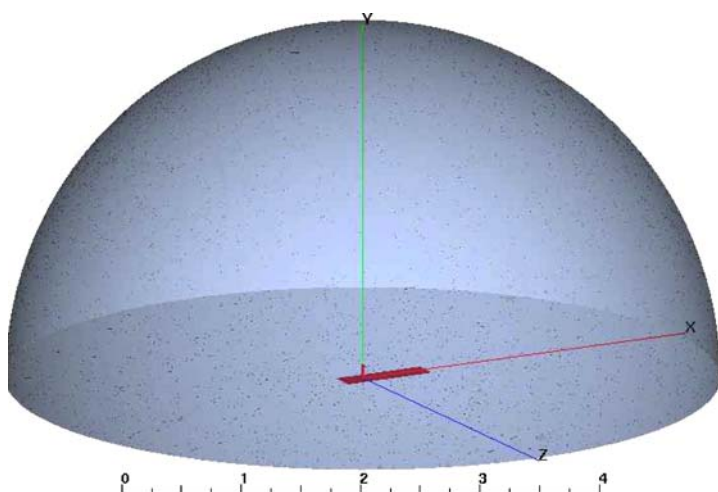


Fig. 4.15 Visualization of complete acoustic grid used for transient computations with radius $r = 3$ m showing coupled region at the center of the domain. Distance scale in meter.

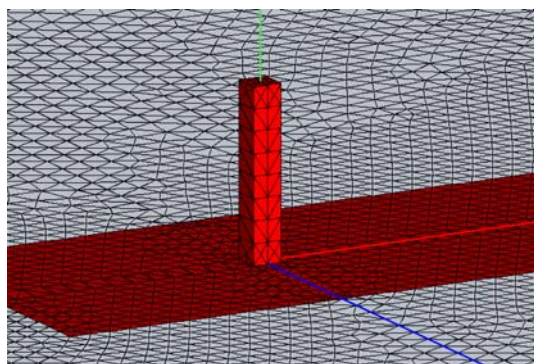


Fig. 4.16 Close up of acoustic grid used for transient computations depicting edges of tetrahedra on the bottom plane and on the cylinder surface.

creases the accuracy of the computation. A spatial discretization has been chosen, in which a ratio of $h_a/h_f = 10$ in the region directly around the cylinder sufficed to produce mesh independent results. Following this discretization criteria three different mesh resolutions have been tested with the number of linear nodes in the coupled region ranging from 8.092 to 24.177. Figure 4.19 presents results for the amplitudes at a radius $r = 1$ m using the three different spatial discretizations. While the finest mesh produces a smoother directivity pattern, for the other grids only minimal differences are observed in the amplitudes, which demonstrates the robustness of our interpolation scheme.

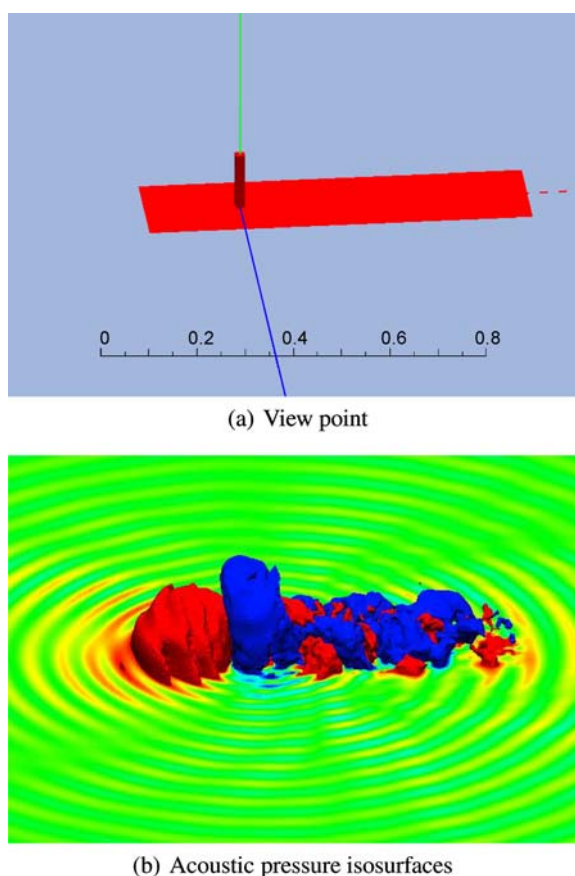


Fig. 4.17 Isosurfaces of acoustic field for values ± 2 Pa at time $t=10$ ms obtained using fluid results from CFX-ANSYS simulations.

Figure 4.20 presents several isosurfaces of the acoustic pressure clipped at yz -plane at the main frequency component present in the computation, $f = 55$ Hz. Values of the isosurfaces range from 5 mPa to 54 mPa, the outermost corresponding to a sound pressure level (SPL) of about 48 dB.

Wall-mounted Cylinder with Elliptic Profile

Similarly as for the square cylinder profile, harmonic acoustic computations have been performed for the case using the profile from Figure 4.12 and its SPL values and directivity pattern have been analyzed. The acoustic sources have been evaluated using the velocity components from the CFD results computed with CFX-ANSYS using SAS turbulence modeling presented in Figure 4.14. The acoustic computation has been performed using a similar configuration for the computational domain as the one depicted in Figure 4.18, except for the cylinder geometry. Figure 4.21 presents a

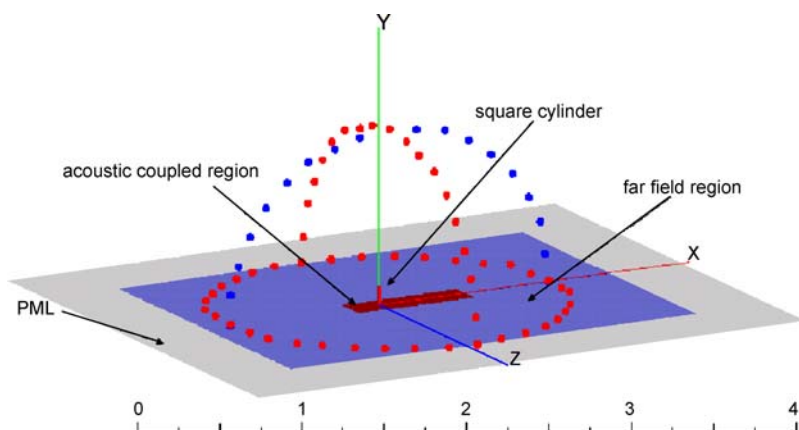


Fig. 4.18 Schematic drawing of the acoustic domain used for the harmonic computation showing points used for directivity analysis. Distance scale in m.

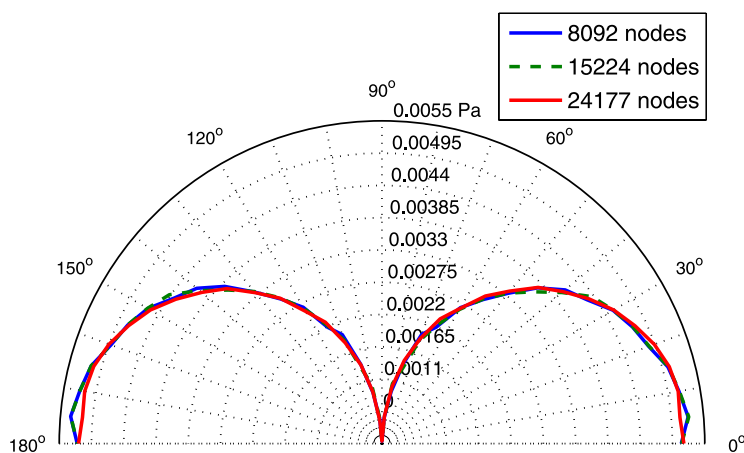


Fig. 4.19 Comparison of amplitudes at radius $r = 1$ m on the crossflow yz -plane using three different spatial discretizations in the acoustic coupled region

close-up of the acoustic grid showing the corresponding elliptic profile employed in this case. Regarding the acoustic coupled region, the fine acoustic sources from the fluid resolution have been interpolated on 21160 hexahedron corner nodes.

In the acoustic computations, the main frequency component found for this problem was $f = 39$ Hz. For this frequency value, isosurfaces of the acoustic pressure clipped at the yz -plane are presented in Figure 4.22. Values of the isosurfaces range from 22 mPa to 100 mPa and the outermost isosurface corresponds in this case to 61 dB and, similarly as in the case using the square cylinder profile, the directivity pattern for this main frequency value results in a dipole-like acoustic field.

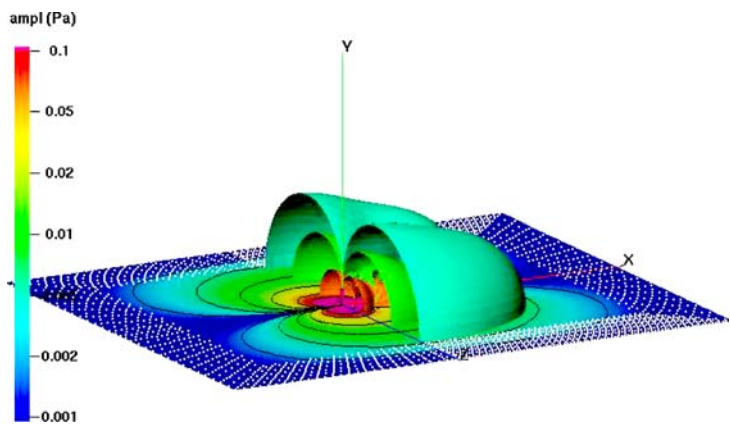


Fig. 4.20 Isosurface of acoustic pressure for wall-mounted square cylinder at $f = 55$ Hz, clipped at yz -plane. Dotted region represents PML.

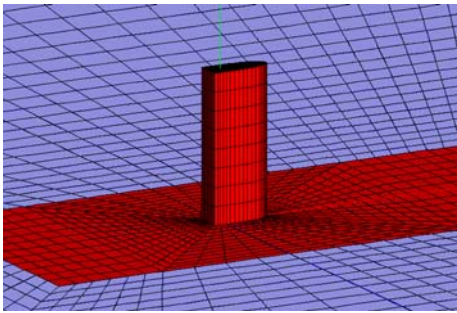


Fig. 4.21 Close up of acoustic grid for the case of the elliptic profile used for harmonic computations

Table 4.2 Comparison of main frequency values found in simulations and measurements

| f_{main} | Square Profile | Elliptic Profile |
|-------------------|----------------|------------------|
| Simulation | 55 Hz | 39 Hz |
| Measurements | 53 Hz | 36 Hz |

Evaluation of 3D Results

In the following, acoustic results from the harmonic computations for the two wall-mounted cylinder profiles are evaluated and compared with experimental results from [25]. Table 4.2 presents the main frequency components found in the computations and the frequency values found in the measurements carried out in an anechoic wind tunnel [25]. In Table 4.3 a comparison of the SPL values between the numerical and the experimental results is presented for both cylinder profiles. It

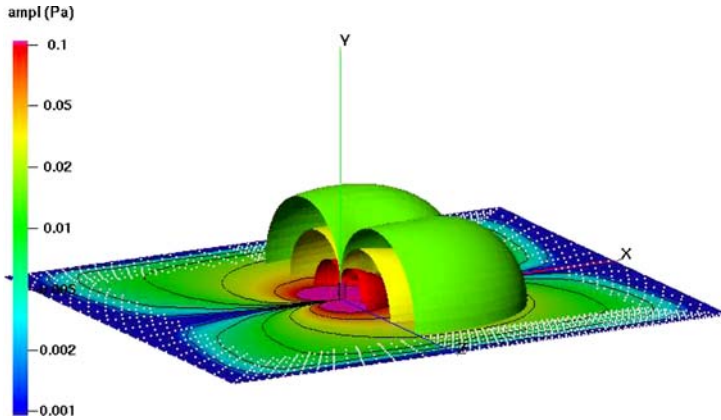


Fig. 4.22 Isosurface of acoustic pressure for wall-mounted square cylinder with elliptic profile at $f = 39$ Hz, clipped at yz -plane. Dotted region represents PML

can be noticed, that for both geometries slightly higher SPL values are obtained in the numerical simulations. At this point it is important to note that, due to practical reasons, in the experimental case the cylinders were mounted at the center of a wall with a crossflow length of $L_{\text{exp}} = 0.66$ m, whereas in the simulation the wall covers the complete domain width $L_{\text{sim}} = 2.22$ m. Reflection of the acoustic waves on the larger wall from the simulation domain is one of the reasons for the higher SPL values at the monitoring points compared. Furthermore, the relative difference of the SPL values from both profiles compare well to the measured value. In Table 4.3 this difference is observed to be 16 dB in the experiments and 14 dB in the numerical computations. Finally, directivity plots of the SPL levels at a radius $r = 1$ m away of the flow-induced noise for the two wall-mounted cylinders are presented in Figure 4.23. In this plot it can be observed the significantly higher amplitudes at all monitoring points obtained in the flow-induced noise computation for the cylinder with elliptic profile.

4.5 Conclusion

The numerical computation of flow induced noise is quite challenging due to the energy and length scale disparity of the flow field compared to the generated acoustic noise. The proposed method applicable to low Mach number problems is based on SAS flow computations and the FE formulation of Lighthill's acoustic analogy. The computation of the acoustic noise due to a flow around wall mounted cylinders with different geometries demonstrate the applicability of the numerical scheme.

Due to the complexity, computational aeroacoustics will remain a challenging topic for research both concerning the mathematical modeling as well as the dedicated numerical methods.

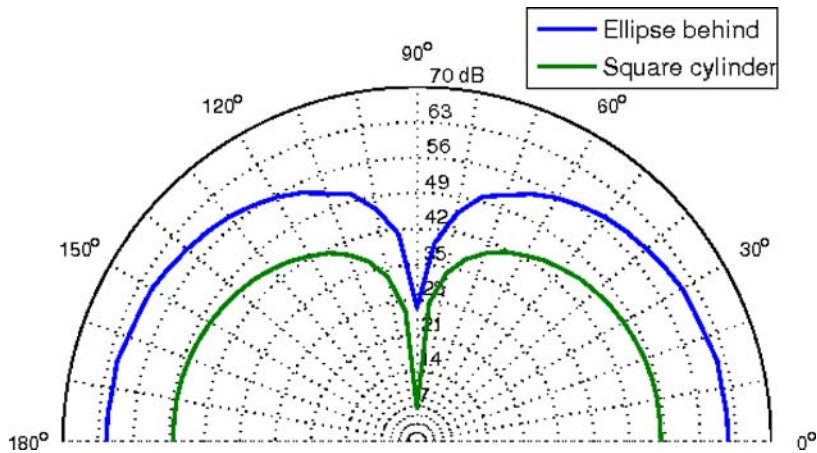


Fig. 4.23 Directivity patterns for two cylinder profiles at radius $r = 1.0$ m on the crossflow yz -plane

Table 4.3 Numerical and experimental SPL values of the flow-induced noise for the two cylinder profiles evaluated at 0° on the yz -plane

| SPL value | Square Profile | Elliptic Profile | Relative SPL difference |
|--------------|----------------|------------------|-------------------------|
| Simulation | 47 dB | 61 dB | 14 dB |
| Measurements | 44 dB | 60 dB | 16 dB |

References

1. Adams RA (1975) Sobolev spaces. Academic Press, New York
2. Ainsworth M (2004) Discrete dispersion relation for hp-version finite element approximation at high wave number. *SIAM Journal of Numerical Analysis* 42:553–575
3. Ali I, Escobar M, Hahn C, Kaltenbacher M, Becker S (2004) Numerical and experimental investigations of flow induced noise around a square cylinder. In: 10th AIAA/CEAS Aeroacoustics Conference, AIAA–2004–3004, Manchester
4. Bhagwat M, Gordon J, (2002) Generalized viscous vortex model for application to free-vortex wake and aeroacoustic calculations. In: 58th Annual Forum of the American Helicopter Society International, Montreal
5. Bogey C, Bailly C, Juvé D (2002) Computation of flow noise using source terms in linearized Euler’s equations. *AIAA Journal* 40:235–243
6. Brentner K, Farassat F (1998) An analytical comparison of the acoustic analogy and Kirchhoff formulation for moving surfaces. *AIAA Journal* 36:1379–1386
7. Breuer M (2001) Direkte numerische Simulation und large-eddy simulation turbulenter Strömungen auf Hochleistungsrechnern. Shaker Verlag, Herzogenrath
8. Cohen G (2001) Higher order numerical methods for transient wave equations. Springer-Verlag, Berlin–Heidelberg
9. Crighton DG (1993) Computational aeroacoustics for low Mach number flows. In: Hardin JC, Hussaini MY (eds) *Computational aeroacoustics*. Springer-Verlag, New York 50–68

10. Curle N (1995) The influence of solid boundaries upon aerodynamic sound. *Proceedings of the Royal Society of London A* 231:505–514
11. Di Francescantonio P (1997) A new boundary integral formulation for the prediction of sound radiation. *Journal of Sound and Vibration* 202:491–509
12. Dumbser M (2005) Arbitrary high order schemes for the solution of hyperbolic conservation laws in complex domains. PhD Thesis, Universität Stuttgart
13. Ekaterinaris J (1999) New formulation of Hardin–Pope equations for aeroacoustics. *AIAA Journal* 37:1033–1039
14. Engquist B, Majda A (1977) Absorbing boundary conditions for the numerical simulation of waves. *Mathematics of Computation* 31:629–651
15. Escobar M (2007) Finite element simulation of flow-induced noise applying Lighthill's acoustic analogy. PhD Thesis, Universität Erlangen–Nürnberg
16. Ewert R, Schröder W (2003) Acoustic perturbation equations based on flow decomposition via source filtering. *Journal of Computational Physics* 188:365–398
17. Farassat F (2001) Acoustic radiation from rotating blades – the Kirchhoff method in aeroacoustics. *Journal of Sound and Vibration* 239:785–800
18. Farassat F, Myers MK (1988) Extension of Kirchhoff's formula to radiation from moving surfaces. *Journal of Sound and Vibration* 123:451–560
19. Ffowcs–Williams JE, Hawkings DL (1969) Sound radiation from turbulence and surfaces in arbitrary motion. *Philosophical Transactions A of the Royal Society* 321–342
20. Fortenbach R (2006) Mehrskalenmodellierung von aeroakustischen Quellen in schwach kompressiblen Strömungen. PhD Thesis, Universität Stuttgart
21. Freund JB, Lele SK, Moin P (2000) Direct numerical simulation of a Mach 1.92 turbulent jet and its sound field. *AIAA Journal* 38:2023–2031
22. Freund JB, Lele SK, Wei M (2004) The robustness of acoustic analogies. In: *Proceedings of the Summer Program, Center for Turbulence Research, Stanford University* 241–252
23. Goldstein ME (1976) *Aeroacoustics*. McGraw–Hill, New York
24. Goldstein ME (2006) A hybrid RANS/LES approach for predicting jet noise. In: *12th AIAA/CEAS Aeroacoustics Conference AIAA–2006–2631*, Cambridge
25. Hahn C, Kaltenbacher M, Lerch R, Becker S, Durst F (2006) Influence of geometry on the generation of aerodynamic noise. In: *Proceedings of the ISMA International Conference on Noise & Vibration, CD-ROM–Proceedings, Leuven* 619–631
26. Hardin JC (1993) Regarding numerical considerations for computational aeroacoustics. In: Hardin JC, Hussaini MY (eds) *Computational aeroacoustics*. Springer–Verlag, New York 216–228
27. Hardin JC, Pope DS, (1994) An acoustic/viscous splitting technique for computational aeroacoustics. *Theoretical and Computational Fluid Dynamics* 6:323–340
28. Hughes TJR (2000) *The finite element method*. Prentice–Hall, Englewood Cliffs
29. Kaltenbacher M (2007) *Numerical simulation of mechatronic sensors and actuators*. Springer–Verlag, Berlin–Heidelberg–New York
30. Joo Lee D, Ok Koo S (1995) Numerical study of sound generation due to a spinning vortex pair. *AIAA Journal* 33:20–26
31. Lighthill MJ (1952) On sound generated aerodynamically. I: General theory. *Proceedings of the Royal Society of London, Series A* 211:564–587
32. Lilley GM (1972) The generation and radiation of supersonic jet noise. Vol IV: Theory of turbulence generated jet noise, noise radiation from upstream sources, and combustion noise. Part II: Generation of sound in a mixing region. Technical Report 4, U.S. Air Force Aeropropulsion Laboratory (AFAPL–TR–72–53)
33. Lilley GM (1974) On the noise from jets. Technical Report, AGARD, CP–131

34. Liow K, Thompson MC, Hourigan K (2001) Computation of acoustic waves generated by a co-rotating vortex pair. In: Proceedings of the 14th Australasian Fluid Mechanics Conference, Adelaide
35. Lockard D (2002) A comparison of Ffowcs Williams–Hawkings solvers for airframe noise applications. In: Proceedings of 8th AIAA/CEAS Aeroacoustics Conference, AIAA–2002–2580, Breckenridge
36. Lyrintzis AS (2003) Surface integral methods in computational aeroacoustics – From the (CFD) near field to the (Acoustic) far-field, *International Journal of Aeroacoustics* 2 2:95–128
37. Manoha E, Herrero C, Ben Khelil S, Guillen P, Sagaut P, Mary I (2002) Numerical prediction of airfoil aerodynamic noise. In: Proceedings of 8th AIAA/CEAS Aeroacoustics Conference, AIAA–2002–2573, Breckenridge
38. Menter F, Egorov Y (2005) A scale adaptive simulation model using two-equation models. In: 43rd AIAA Aerospace Sciences Meeting and Exhibit, AIAA–2005–1095, Reno
39. Mitchell B, Lele SK, Moin P (1995) Direct computation of the sound from a compressible co-rotating vortex pair. *Journal of Fluid Mechanics* 285:181–202
40. Möhring W (1978) On vortex sound at low Mach number. *Journal of Fluid Mechanics* 85:685–691
41. Müller EA, Obermeier F (1967) The spinning vortices as a source of sound. In: Proceedings of the Conference on Fluid Dynamics of Rotor and Fan Supported Aircraft at Subsonic Speeds (AGARD CP–22) 22.1–22.8
42. Oberai A, Ronaldkin F, Hughes TJR (2000) Computational procedures for determining structural–acoustic response due to hydrodynamic sources. *Computer Methods in Applied Mechanics and Engineering* 190:345–361
43. Oberai A, Ronaldkin F, Hughes TJR (2002) Computation of trailing-edge noise due to turbulent flow over an airfoil. *AIAA Journal* 40:2206–2216
44. Paliath U, Morris PJ (2005) Prediction of jet noise from circular beveled nozzles. In: Proceedings of the 11th AIAA Aeroacoustics Conference AIAA–2005–3096, Monterey
45. Peters MCAM (1993) Aeroacoustic sources in internal flows. PhD Thesis, Eindhoven University of Technology, Eindhoven
46. Ribner HS (1996) Effect of jet flow on jet noise via an extension to the Lighthill model. *Journal of Fluid Mechanics* 321:1–24
47. Schram C, Anthoine J, Hirschberg A (2005) Calculation of sound scattering using Curle’s analogy for non-compact bodies. In: Proceedings of the 11th AIAA Aeroacoustics Conference, AIAA–2005–2836, Monterey
48. Scully MP, (1975) Computation of helicopter rotor wake geometry and its influence on rotor harmonic loads. MIT Publications ARSL TR 178–1, Cambridge
49. Seo J, Moon Y (2006) Linearized perturbed compressible equations for low Mach number aeroacoustics. *Journal of Computational Physics* 218:702–719
50. Tam CKW, Webb JC (1993) Dispersion–relation–preserving finite difference schemes for computational acoustics. *Journal of Computational Physics* 107:262–281
51. Uitzmann JT, Schwartzkopff T, Dumbser M, Munz CD (2006) Heterogeneous domain decomposition for CAA. *AIAA Journal* 44:2234–2250
52. Uzun A, Lyrintzis AS, Blaisdell GA (2004) Coupling of integral acoustics methods with LES for jet noise prediction. In: Proceedings of AIAA Aerospace Sciences Meeting and Exhibit, AIAA–2004–0517 Reno
53. Wagner C, Hüttl T, Sagaut P (eds) (2007) Large-eddy simulation for acoustics. Cambridge University Press, New York